nature communications

Article https://doi.org/10.1038/s41467-025-60840-z

Cascade reactors for long-life solid-state sodium–air batteries

Received: 26 September 2024

Accepted: 4 June 2025

Published online: 01 July 2025

Check for updates

Xue Sun[1,2,3], Haitao Li[1,4], Yajie Song[1], Jiaxuan Liu[1], Pengxiang Ji[2], Xincheng Lei[2], Xiangzhi zhang[4], Qingsong Liu[1], Menglu Li[1], Biao Deng[4], Dong Su[2] ✉ & Jiajun Wang[1,3] ✉

Sodium (Na)-air batteries show significant potential as alternatives to lithium-air batteries due to their high theoretical energy density and the abundant availability of sodium reserves. Nevertheless, the formation of complex products, specifically NaO_2, Na_2O_2, $Na_2CO_3·xH_2O$, during the multi-step reactions inevitably raises reconciled potential incompatibility that causes low efficiency and large overpotential. Here, we introduce a cascade electrocatalysis strategy that involves switchable metal and oxygen redox chemistry through electrochemical potential tuning. Leveraging the lithium ion spatial pinning effect, sodium ions trigger in the $Na[Li_{1/3}Ru_{2/3}]O_2$ electrode system to toggle the geometric state at a low electrochemical potential and oscillate among different catalytic states to achieve sequential conversion of complicated multi-step intermediates. The $Na[Li_{1/3}Ru_{2/3}]O_2$ catalyst effectively compartmentalizes the threshold potential that circumvents deactivating or competing pathways while coupling different catalytic cycles. As a result, the sodium-air battery employing this catalyst exhibits long-term reversibility over 1000 cycles with a decent catalysis efficiency exceeding 99%. Our results demonstrate that the cascade electrocatalysis strategy contributes to the design of integrated sodium-air batteries with long-term cycling stability.

Na-air batteries have garnered considerable attention as a promising and affordable energy storage solution owing to the abundance of sodium resources and high theoretical energy density[1]. However, the inadequate cycling stability of Na-air batteries, particularly on the electrode side, hinders their widespread implementation. Specifically, the reduction of O_2 involves a multi-electron process, yielding multiple products such as NaO_2, Na_2O_2, and $Na_2CO_3·xH_2O$. While most electrode candidates exhibit selective catalysis for NaO_2 conversion, they struggle to efficiently convert all products due to decomposing Na_2O_2 and $Na_2CO_3·xH_2O$ challenges, which consequently limit the cycling reversibility of a Na-air batteries[2–4]. To address this limitation, an ideal catalyst must moderate binding strength with multiple intermediates and promote their adsorption-desorption efficiency. Transition metal oxides (TMO), exemplified by RuO_2[5], have recently emerged as promising catalysts in air batteries due to their abundant *d* orbitals and diverse valence distributions[6,7]. Nevertheless, TMO typically provides a single active center due to the fixed crystal structures, which is too limited for coupling electrons with adsorbates[8–10]. To overcome this challenge, designing two (or more) different reactive states of TMO is plausible to equilibrate the adsorption coverage of products and achieve high cycling stability in Na-air battery systems.

Cascade catalysis is an effective methodology for streamlining the multi-step conversion of complex products within a single reaction process through applying external stimuli[11–13]. Recently, with the light

---

[1]MOE Engineering Research Center for Electrochemical Energy Storage and Carbon Neutrality in Cold Regions, School of Chemistry and Chemical Engineering, Harbin Institute of Technology, Harbin, China. [2]Beijing National Laboratory for Condensed Matter Physics, Institute of Physics, Chinese Academy of Sciences, Beijing, PR China. [3]National Key Laboratory of Chemical and Physical Power Sources, Tianjin Institute of Power Sources, Tianjin, PR China. [4]Shanghai Institute of Applied Physics, Chinese Academy of Sciences, Shanghai, China. ✉e-mail: dongsu@iphy.ac.cn; jiajunhit@hit.edu.cn

trigger, the alternatively changed TM-O bond has been proved to promote the oxygen evolution reactions (OER) efficiency by continuously regulating O-H bond cleavage and O-O bond formation[11–13]. Applying this cascade catalytic strategy to Na-air batteries requires two key design principles: dynamic active sites during cycling and alignment of electrochemical potential with redox components. Given the diversity of species generated during charging, active sites must adapt to the evolving redox process at varying voltages[14]. One approach is utilizing Na-containing layered oxides as catalysts, where Na ion extraction is voltage-dependent. From the perspective of *d*-band theory[3], the *d*-electron-pair wave function properties of 4*d*/5*d* transition metal elements with a large spatial extent may offer opportunities for modulating the electronic structure to boost the catalytic activity. Then, Na^+ electrochemical intercalation can induce various valence states in TM ions, allowing for tunable electronic and redox properties. Moreover, aligning active sites with the distinct electrochemical potentials of NaO_2, Na_2O_2, and their hydrates could maximize energy efficiency while minimizing parasitic reactions[15–17]. Although this strategy promises to enable the efficient multi-step reaction sequences, implementing this strategy and tuning electrochemical potentials in a Na-air battery remains poorly understood[18].

In this study, we have synthesized a layered TMO catalyst, $Na[Li_{1/3}Ru_{2/3}]O_2$, to facilitate the cascade conversion of mixed intermediates within Na-air batteries. The hybridization of the Ru-O bond in $Na[Li_{1/3}Ru_{2/3}]O_2$, as illustrated in Fig. 1a, can be controlled by regulating alkali ions in the Ru layer. Accompanied by the variation of potential, the oriented orbital hybridizes in two axes between TM and O, resulting in varying degrees of the metal *d* band and oxygen *p* band broadening. Consequently, the catalyst with a different extent of *d*-*p* band broadening covers the intermediate and promotes the adsorption-desorption efficiency. This modification results in enhanced electron transfer efficiency at high electrochemical potentials and initiates the formation of dynamic TM active centers for sequential catalysis. The unit cell in the coupled integrated catalysis undergoes reversible geometric conversion of RuO_6 with Li^+ as spatial localization, promising the structural stability of the material. This modification results in enhanced electron transfer efficiency at high electrochemical potentials and initiates the formation of dynamic TM active centers for sequential catalysis. Consequently, the Na-air cell using $Na[Li_{1/3}Ru_{2/3}]O_2$ as electrode exhibits an energy conversion efficiency exceeding 99%, coupled with a high discharge capacity of 15,000 mAh g^{-1}. Furthermore, it demonstrates long-term reversibility over 1000 cycles with a minimal overpotential of 0.75 V. Compared with RuO_2, $Na[Li_{1/3}Ru_{2/3}]O_2$ showcases switchable active centers with good reversibility in electrochemical reactions. Notably, the catalysts present highly distinguishable threshold potentials for multiproduct decomposition in Na-air batteries, favoring the avoidance of deactivation or competing pathways. The sequential arrangement of potential windows, influenced by the dynamic transition metal valence state, could provide a practical framework for improving the performance of metal-air batteries.

Results

Sequential catalysis for improved rechargeability

The layered microparticles $Na[Li_{1/3}Ru_{2/3}]O_2$ with a disordered TM/Li-intralayer arrangement were prepared by one-step solid-state reactions[19] (Supplementary Fig. 1). The X-ray diffraction (XRD) pattern of $Na[Li_{1/3}Ru_{2/3}]O_2$ and Rietveld refinement show that the adopts an O3-type layered structure (Supplementary Fig. 2 and Table S1). Na ions are situated within the AM (Alkali metal) layer, while a disordered Li/TM arrangement exists in the TM (transition metal) layer, delivering a Na–O–Li configuration[20]. Inductively coupled plasma optical emission spectroscopy (ICP-OES) affirms that the chemical composition of $Na[Li_{1/3}Ru_{2/3}]O_2$ is consistent with the expected stoichiometry ratio (Supplementary Table 2).

A quasisolid-state polymer electrolyte (QPE) that consists of PVDF–HFP–10% SiO_2–$NaClO_4$–tetraethylene glycol dimethyl ether (TEGDME) as an electrolyte (Supplementary Fig. 3 and Fig. 4), both $Na[Li_{1/3}Ru_{2/3}]O_2$ and commercial RuO_2 were then utilized as catalysts for solid-state Na-air batteries (SSNAB) to evaluate the catalytic performances. In galvanostatic tests, $Na[Li_{1/3}Ru_{2/3}]O_2$ indicates a low discharge-charge overpotential of 0.75 V while demonstrating a favorable discharge capacity of 15,000 mAh g^{-1} (Fig. 2a). As a reference, the commercial RuO_2 catalyst has a high OER overpotential (0.97 V) with a poor discharge capacity (8500 mAh g^{-1}). In contrast, the $Na[Li_{1/3}Ru_{2/3}]O_2$ catalyst exhibits a considerably higher energy

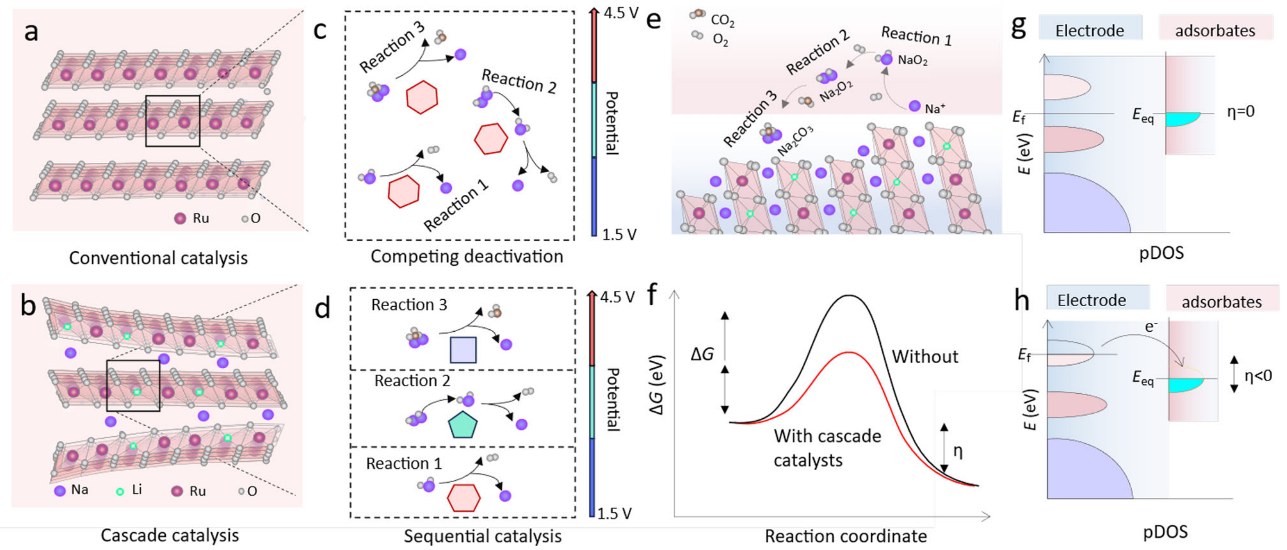

Fig. 1 | Schematic illustration of cascade catalysis for Na-air battery. **a**, **b** Ion-insertion catalysts may be more likely to induce cascade catalytic effects than conventional catalysts. **c**, **d** The cascade catalytic strategy to Na-air batteries requires two key design principles: dynamic active sites during cycling and alignment of electrochemical potential with redox components (Reaction 1–3). **e** Schematic illustration of electrochemical reactions of Na-air batteries at electrode–electrolyte interfaces, cascade catalytic strategy promises to enable the efficient multi-step reaction sequences. **f** The kinetic barrier of a reaction (ΔG) can be reduced owing to cascade catalysis. **g**, **h** Cascade catalysis changes the thermodynamic electrochemical driving force of the reaction ($\eta = E_F - E_{eq}$, where E_F is the Fermi level of the electrode and E_{eq} is the Fermi level of the reactant): pDOS, partial density of states.

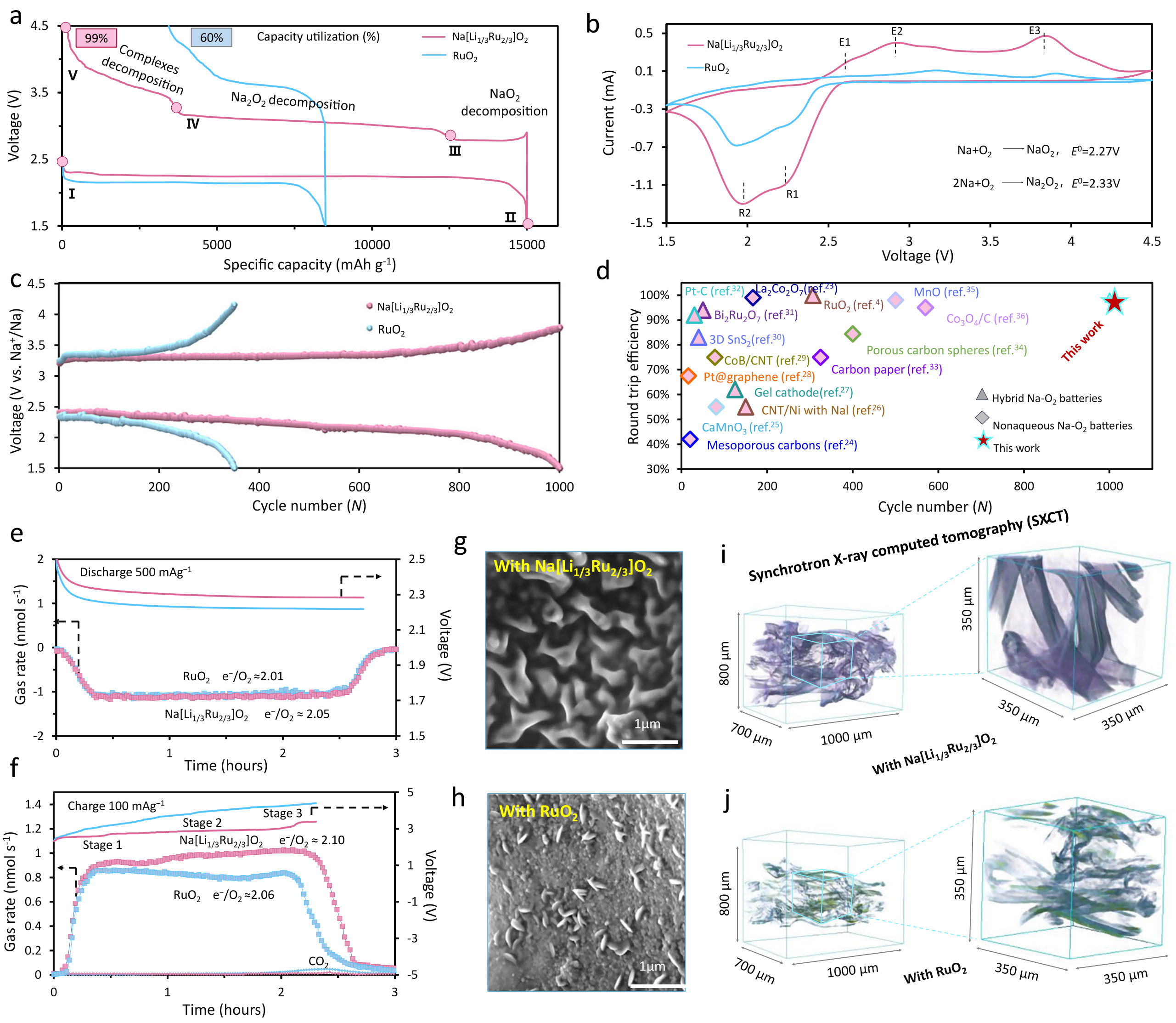

Fig. 2 | Electrochemical performances of SSNAB. a Galvanostatic curves of SSNAB based on commercial RuO_2 and $Na[Li_{1/3}Ru_{2/3}]O_2$ sample at a current density of 100 mA g^{-1}. **b** Contrast CV curves with the aforementioned two catalysts between 1.5 and 4.5 V, scan rate: 0.1 mV s^{-1}. **c** The cycling performance with a 500 mAh g^{-1} capacity limitation. **d** The comparison with other notable published studies on the cycling performance of sodium-oxygen battery systems, the source of the literature data shown in this figure can be found in Supplementary Table 3. **e**, **f** In situ DEMS analysis of the gas consumption (**e**) and evolution (**f**) during SSNAB operation with RuO_2 and $Na[Li_{1/3}Ru_{2/3}]O_2$ electrodes. **g**, **h** SEM image of discharged electrode morphologies obtained after a full discharge during the galvanostatic test conducted at a current density of 100 mA g^{-1}, as shown in Fig. 2**a**. **i**, **j** Synchrotron x-ray tomography reconstruction of discharged electrode utilizing volume rendering.

efficiency (over 99%) compared to the RuO_2 catalyst (60%). Furthermore, both the two catalysts show similar discharge profiles with a single plateau at 2.3 V. Whereas, there are three different charging plateaus with $Na[Li_{1/3}Ru_{2/3}]O_2$ catalyst at (i) C2.5 V, (ii) C3.5 V, and (iii) C4.5 V, respectively. It is known that plateau (i) originates from superoxide decomposition, and plateaus (the other two) can be ascribed to the decomposition of the peroxide phase and the byproduct, respectively[21]. These results verify that the high $Na[Li_{1/3}Ru_{2/3}]O_2$ activity could be attributed to the separation of reaction potentials. To further study the potential-dependent oxidation kinetics, the cyclic voltammetry (CV) of the two catalysts was collected (Fig. 2b). Compared with the multiple redox peaks of the RuO_2 plots, $Na[Li_{1/3}Ru_{2/3}]O_2$ catalyst also shows a multistage redox process. The larger redox current and more negligible polarization indicate that $Na[Li_{1/3}Ru_{2/3}]O_2$ catalyst can tune redox reaction potential, which is essential for mediating the reaction kinetics[22,23].

The difference in cycling stability between RuO_2 and $Na[Li_{1/3}Ru_{2/3}]O_2$ corroborates the cascade catalyst effect in the SSNAB. At a consistent capacity of 500 mAh g^{-1}, the $Na[Li_{1/3}Ru_{2/3}]O_2$ electrodes maintain stable discharge and charge voltages without significant degradation even after 1000 cycles, while the reaction voltage of RuO_2 decreased after 350 cycles due to intense OER polarization (Fig. 2c). In addition, $Na[Li_1/_3Ru_2/_3]O_2$ and RuO_2 electrodes were further tested for stability at a high current density of 500 mA g^{-1}, with a capacity limit of 1000 mAh g^{-1}. Notably, the $Na[Li_1/_3Ru_2/_3]O_2$ exhibited a stable specific capacity and maintained a discharge voltage above 1.5 V after 550 cycles. In contrast, RuO_2 showed significant degradation after only 120 cycles (Supplementary Fig. 5). The satisfied cycle stability and energy efficiency of $Na[Li_{1/3}Ru_{2/3}]O_2$ electrodes show substantial advantages over previous reports of sodium-oxygen battery systems[4,23–36] (Fig. 2d and Supplementary Table 3). These observations demonstrate that $Na[Li_{1/3}Ru_{2/3}]O_2$ can be a suitable catalyst for coupling multiple consecutive catalytic reactions (Supplementary Figs. 6 and 7).

In ambient conditions, the pouch-type battery measures 10 × 10 cm^2 and achieves a capacity of 650 mAh at 4.5 A. Its impressive cycling stability over 40 cycles highlights the potential of $Na[Li_1/_3Ru_2/$

$_{3}]O_2$ for large-scale Na–air battery applications (Supplementary Fig. 8). The flexible pouch-type solid-state Na-air battery can constantly power a micro-robot, indicating the great prospect of the $Na[Li_{1/3}Ru_{2/3}]O_2$ in promoting the practical application of Na-air batteries (Supplementary Fig. 9). These results suggest the importance of the $Na[Li_{1/3}Ru_{2/3}]O_2$ in constructing a highly safe and stable. To investigate whether the redox potential of the catalyst aligns with the voltage window of Na-air batteries, charge and discharge tests of $Na[Li_{1/3}Ru_{2/3}]O_2$ and RuO_2 as electrodes were conducted in an Ar atmosphere. The charge-discharge curves of $Na[Li_1/_3Ru_2/_3]O_2$ revealed significant oxygen redox processes. In contrast, RuO_2 lacked effective redox activity and alignment with the sodium-oxygen battery voltage window, limiting its effectiveness as a cascade catalyst for energy efficiency optimization. (Supplementary Fig. 10).

To further understand the discharge-charge mechanism, the gas evolution was probed with in situ DEMS analysis (Fig. 2e, f). During discharge-charge processes, the $e^-/O_2 > 2$ ratios of $Na[Li_{1/3}Ru_{2/3}]O_2$ can be obtained, which suggests that more than one electron is transferred or multiple steps are involved in the complex electrode reaction[37]. Scanning electron microscopy (SEM) was employed to understand the specific morphology of the discharge products. (Fig. 2g, h). The two distinct forms of the deposited product (nanorod-like products for RuO_2 and thin-layer ones for $Na[Li_{1/3}Ru_{2/3}]O_2$) indicate a strong correlation between electrode surfaces and the thermodynamics/kinetics of product deposition. Using the high spatial resolution and high contrast of synchrotron X-ray computed tomography, the active components in the electrode can be separated from the reaction products, enabling the examination of the product formation and decomposition processes[38]. The reconstructed 3D volume rendering images of coexisting products with $Na[Li_{1/3}Ru_{2/3}]O_2$ (Displayed in purple) precipitate massively within the electrode with a homogeneous distribution. Additionally, the green 3D visualization image roughly retrieved the scattered product distribution in the RuO_2 electrode (Fig. 2i, j). The 3D analysis measures the volume variation of the deposited products between the electrodes above (Supplementary Fig. 11), indicating that electrochemical ion insertion may lead to uniform product deposition by expanding the electrochemically active surface area beyond the electrode-electrolyte interface in the host material[39].

Spatiotemporal control of complicated products

SEM and Time-of-flight secondary ion mass spectrometry (TOF-SIMS) further analyzed the morphological evolution of the discharge/charge products to explore the underlying catalysis process (Fig. 3a). At stage I, typical micrometer-scale cubic products of NaO_2, approximately 1 µm in size, were observed randomly scattered on the surface of $Na[Li_{1/3}Ru_{2/3}]O_2$ (Fig. 3b). Following stage II, many nanorod-like products of $Na_{2\text{-}x}O_2$ and a few aggregated particles (Na_2CO_3) appear on the $Na[Li_{1/3}Ru_{2/3}]O_2$ surface. TOF-SIMS images show the in-plane and 3D distribution of the Na^- signal at the various potentials (Fig. 3a and Supplementary Fig. 12)[40]. The color bar from black to white represents the relative intensity variation of the Na^- signal. The distribution and size of these white particles are similar to those of product particles in the SEM images (Fig. 3c). Furthermore, SEM images of stages III–V confirmed that most cubic and nanorod-shaped products gradually decompose. As the charging progresses, the Na^- signal intensity gradually decreases in stages III–V, indicating that there were almost no residual oxygen-containing products in the electrode post-charging at a fully charged electrode. This is consistent with the TOF-SIMS depth profile results (Supplementary Fig. 13). In contrast, for commercial RuO_2 electrodes, the sporadic products during the discharge process and the incomplete decomposition of products after charging indicate their inferior catalytic capability (Supplementary Fig. 14).

The enhancement of catalytic activity could be associated with the hierarchical architecture of the catalyst. $Na[Li_{1/3}Ru_{2/3}]O_2$ catalyst may undergo structural transformation and play a dynamic catalytic effect. Therefore, ex-situ XRD is employed to inquiry the electronic and configurational evolution of $Na[Li_{1/3}Ru_{2/3}]O_2$ at one catalysis cycle (Supplementary Fig. 15). In the discharged state (stage II), several new diffraction peaks are attributed to the formation of NaO_2 (JCPDS 77-0207), Na_2O_2 (JCPDS 74-0895), and parasitic product Na_2CO_3 (JCPDS 77-2082), respectively[41]. During the subsequent charge process (stage III–V), the (003) diffraction peak of $Na[Li_{1/3}Ru_{2/3}]O_2$ continuously shifts owing to the $O3 - O1' - O1$ phase change[42]. The intensity of all diffraction peaks from NaO_2, Na_2O_2, to Na_2CO_3 gradually weakens and completely disappears at the end of the charging process. The high-resolution XPS spectra obtained for the O 1 s region of the fully discharged electrodes, revealed Na_2O_2 is the main discharge product accounts for approximately 47.6% (Supplementary Fig. 16). The phase transition reveals that the reductive coupling mechanism may occur at high voltage regions for TM, favoring the activation of new O redox-active centers for sequential catalysis.

The progression of the electrode reaction during the cycled system was further disclosed in detail with Raman analysis. Fig. 3d shows two typical Raman vibration shifts of 485 and 595 cm^{-1} at the pristine electrode (I), which can stem from the O-Ru-O bending (E_g) and another Ru-O stretching (A_{1g}) in $Na[Li_{1/3}Ru_{2/3}]O_2$, respectively[43]. After discharge (stage II), the additional peaks are observed at 1107 cm^{-1} and 1146 cm^{-1} (O_2^{-*},NaO_2), 800 cm^{-1} (Na_2O_2), and additional 1080 cm^{-1} (Na_2CO_3)[44]. During charging (stage III-V), the vibration of E_g and A_{1g} of $Na[Li_{1/3}Ru_{2/3}]O_2$ gradually weakened, and the vibration peaks from NaO_2, Na_2O_2 to Na_2CO_3 gradually disappeared. At high potential (stage V), the new Raman vibration of peroxo-species $(O_2)^{n-}$ at 850 cm^{-1} and superoxide-species O-O bond at around 1100 cm^{-1} was observed in charged $Na[Li_{1/3}Ru_{2/3}]O_2$[45]. The results unequivocally validate that the reversible evolution of composite products is closely related to the structural changes of $Na[Li_{1/3}Ru_{2/3}]O_2$. Potential-driven formation of $(O_2)^{n-}$ species in catalysts may contribute to dramatic promotion in the catalytic activity.

To further elucidate the chemical compositions of the $Na[Li_{1/3}Ru_{2/3}]O_2$ electrodes, O *K*-edge XAS spectra were obtained (Fig. 3e). Three distinct absorption peaks at 532.0, 532.9, and 534.4 eV can be identified, corresponding to NaO_2, Na_2O_2, and Na_2CO_3, respectively. Additionally, a substantial amount of Na_2CO_3 can be fully decomposed even after charging 4.5 V. These findings align well with the previously discussed XRD and Raman results. In contrast, for the structurally stable RuO_2 catalyst, the XRD analyses indicate the presence of undecomposed byproducts after deep charging (Supplementary Fig. 17). The Distribution of Relaxation Times model deriving from the EIS spectra also proves the above conclusion. (Supplementary Figs. 18 and 19 and Table 4).

Structural reversibility

A cascade pathway driven by electrochemical potential has been substantiated for $Na[Li_{1/3}Ru_{2/3}]O_2$ serving as switchable electrocatalysts for the SSNAB. Hence, it is crucial to comprehend the underlying mechanism of its electrochemical reversibility. The inherent 3D-disordered cationic framework of $Na[Li_{1/3}Ru_{2/3}]O_2$ could stabilize structures at highly charged states (Fig. 4a). High-angle annular dark field-scanning transmission electron microscopy (HAADF-STEM) further validated the O3-type structure of pristine $Na[Li_{1/3}Ru_{2/3}]O_2$ with lattice spacings of 0.527 nm (Fig. 4b and Supplementary Fig. 20). Furthermore, the O1 phase along the [010] plane is captured at the 4.5 V-charged state (Supplementary Fig. 21a)[46]. No noticeable contrast change was observed in the Na layers, which aligns closely with the limited migration of Ru ions to the Na sites at a charge of 4.5 V. Therefore, Na ions of $Na[Li_{1/3}Ru_{2/3}]O_2$ always occupy the octahedral sites in the Na layer instead of prismatic sites. TM/Na sites are aligned on top of each other. The O3-type layered structure of pristine $Na[Li_{1/3}Ru_{2/3}]O_2$, which was also preserved in the samples discharged to 1.5 V

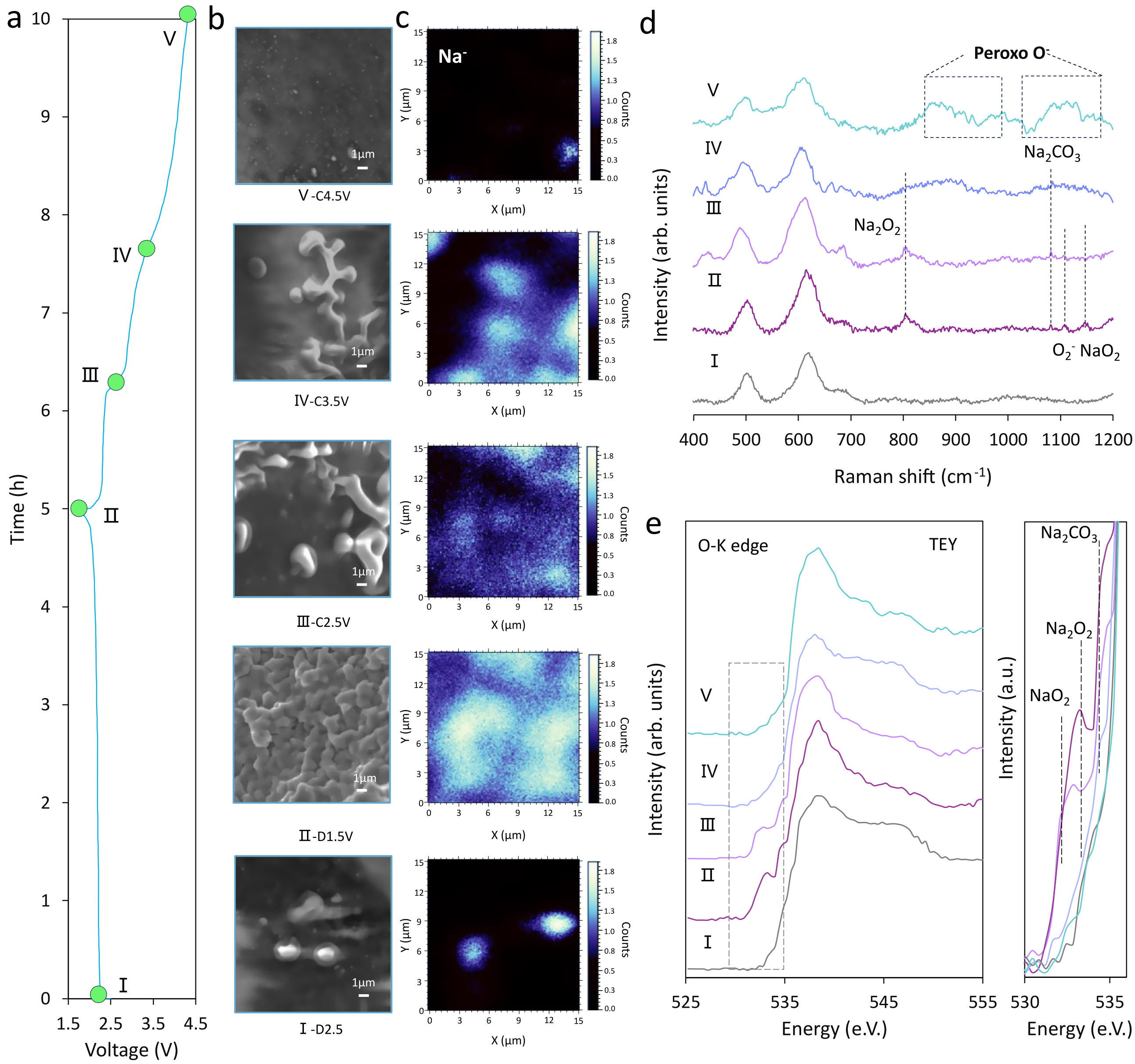

Fig. 3 | Electrode reaction process in the presence of Na[Li$_{1/3}$Ru$_{2/3}$]O$_2$. **a** Charge–discharge profile at a current density of 200 mA g^{-1}, with a capacity limit of 1000 mAh g^{-1} corresponding to **b** Ex-situ SEM analyses, and **c** corresponding the TOF-SIMS of element mappings of Na$^-$ secondary ion distribution on the surface of cycled Na[Li$_{1/3}$Ru$_{2/3}$]O$_2$ electrodes. **d** Ex situ Raman spectra of Na[Li$_{1/3}$Ru$_{2/3}$]O$_2$ at the different voltage states in the SSNAB. **e** O *K*-edge XAS under the TEY pattern for cycled Na[Li$_{1/3}$Ru$_{2/3}$]O$_2$ electrode.

(Supplementary Figs. 21b and 22). Furthermore, the phase transition of O3 – O1′ – O1 could minimize the electrostatic repulsions between Na and TMs. Therefore, the appearance of O1′ and O1 intermediate phases is crucial to trigger the anionic redox and enable the reversible oxygen evolution.

The voltage-dependent structural and chemical transformations for Na[Li$_{1/3}$Ru$_{2/3}$]O$_2$ are investigated by spectroscopy characterizations. The Ru *N*-edge electron energy loss spectra (EELS) of charged Na[Li$_{1/3}$Ru$_{2/3}$]O$_2$ at 4.5 V display a redshift (Fig. 4c) as one moves from the bulk to the surface, indicating that Ru is oxidized at the surface. Additionally, the pre-edge peak transfers 0.5 eV to a higher energy level from the bulk to the surface for the O K-edge, consistent with previous reports regarding the presence of O$_2^{n-}$ species[47].

To further examine the electron-spin configurations of the catalysts, ex-situ magnetic susceptibility experiments were performed on Na[Li$_{1/3}$Ru$_{2/3}$]O$_2$ samples at various charge and discharge states from 0 to 200 K (Fig. 4d and Supplementary Table 5). The pristine sample exhibited an effective magnetic moment (μ_{eff}) of about 2.78 μeff, indicating high spin ($t_{2g}^3e_g^1$) Ru^{4+}. In contrast, the charged sample showed a sharp decrease in μeff to 1.45 μ_{eff}, suggesting low-spin Ru^{5+} and internal charge transfer between Ru and O during oxidation[48]. Considering the empty e_g orbitals in higher energy levels, the electronic hopping between half-filled t_{2g} levels and unoccupied eg levels leads to ferromagnetic behavior. This implies the involvement of anions in the redox activity of Na[Li$_{1/3}$Ru$_{2/3}$]O$_2$, as the coupling of lone-pair electrons on Ru and O gradually reduces the cell's overall magnetization. Additionally, changes in electrochemical potential can influence orbital occupation, regulating the dynamic catalytic process that relies on electron orbital occupancy[49]. The EPR measurements and projected density of states (DOS) also support this conclusion (Supplementary Figs. 23 and 24).

To uncover the origin of the structural reversibility, the chemical environment of Li was investigated to reveal its effect on electron and lattice alteration. The ^{7}Li solid-state NMR spectra illustrated two

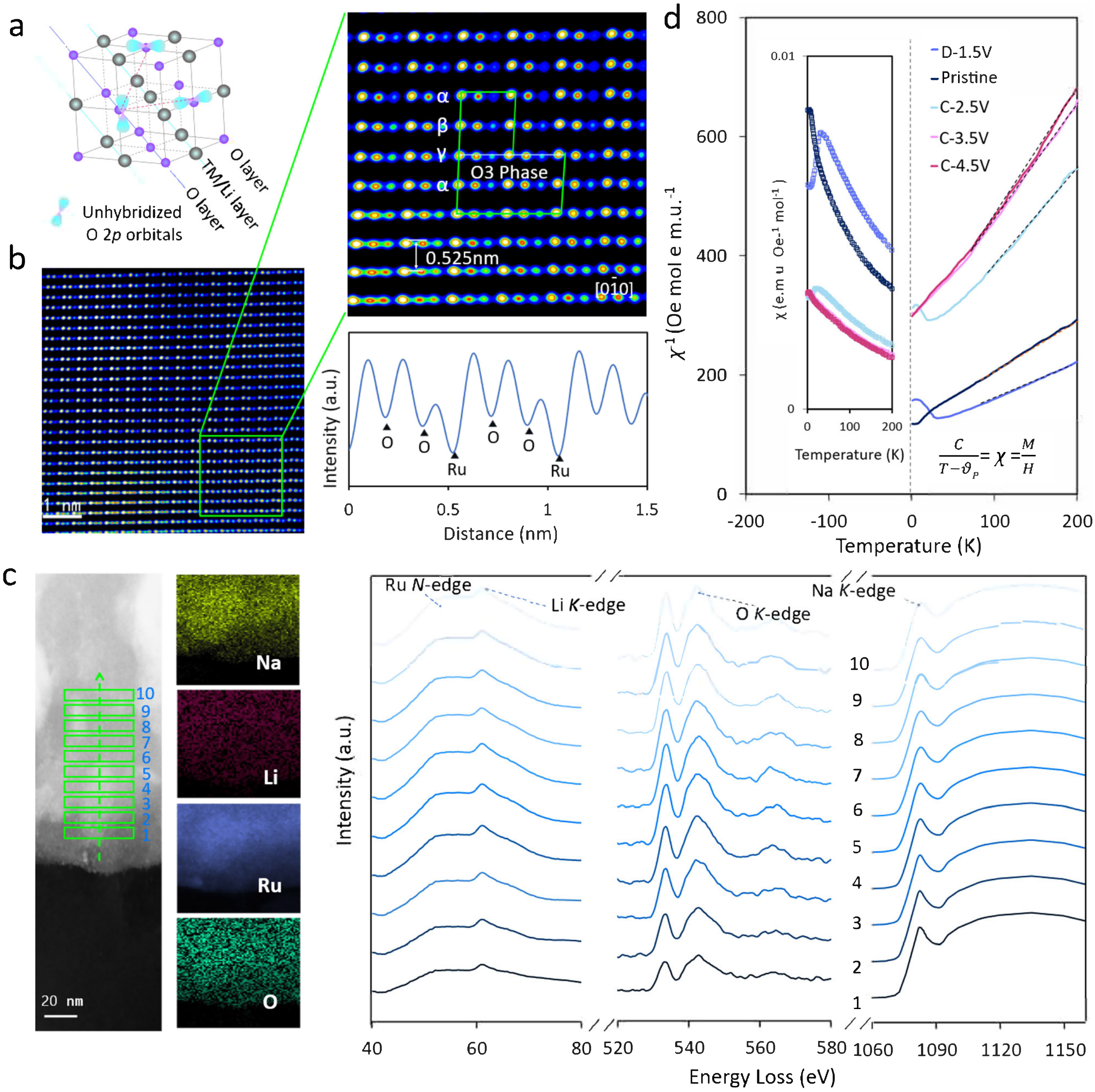

Fig. 4 | The reversible evolution of catalyst structure upon cycling. a 3D-disordered cation framework of Na[$Li_{1/3}Ru_{2/3}$]O_2 with randomly distributed unhybridized O 2p orbitals. **b** HAADF-STEM images and crystal structure diagram of Na[$Li_{1/3}Ru_{2/3}$]O_2 along the [010] zone axis, showing layer spacings for pristine Na[$Li_{1/3}Ru_{2/3}$]O_2. **c** STEM-HAADF image and corresponding EELS spectra from the selected regions in C-4.5 V of Na[$Li_{1/3}Ru_{2/3}$]O_2. **d** Reciprocal susceptibility χ^{-1}, with dashed lines indicating linear fits per the Curie–Weiss law; inset shows the temperature dependence of magnetic susceptibility in the Na[$Li_{1/3}Ru_{2/3}$]O_2-cycled system.

signals at around 150 and 800 ppm, which are ascribed to Li^+ within the alkali metal layers (Li_{AM}) layer and the pristine sample's transition metal layer (Li_{TM}), respectively[50]. Following charging to 4.5 V, almost all the Li ions reside in the AM layer, suggesting the migration of Li_{TM} into the AM layer. The migrated Li into the AM layer could resist lattice gliding by the "pinning effect", ensuring excellent structure endurance. Furthermore, when discharging to 1.5 V, a reversible migration of Li contributes to stabilizing the crystalline structure (Supplementary Fig. 25a). According to the ^{23}Na NMR spectra (Supplementary Fig. 25b), Na migration within the AM layers of Na[$Li_{1/3}Ru_{2/3}$]O_2 delivers a reversible evolution, enhancing the reversibility of the Na–O–Li (Fig. 4f)[51]. In addition, Na[$Na_1/_3Ru_2/_3$]O_2 as a reference sample further confirms the key role of Li^+ in the sodium-air battery electrode (Supplementary Figs. 26–28). According to the reference model put forth by ref. 52, We can justifiably ascribe the variations in migration mechanisms to the existence of lone-pair electrons in the t_{2g} and e_g occupation orbitals of TM. Given this evidence, we conclude that the reversible redox process, as an external stimulus, could tune the electronic state of catalysis for the sequential electrocatalysis reaction process.

Switchable metal and oxygen redox center

The interplay between structural evolution and cascade catalysis is explored in one catalysis cycle of battery operation with layered Na[$Li_{1/3}Ru_{2/3}$]O_2. We select five state-of-charge (SOC) states, namely the pristine state(I), 2.5 V(II), 3.5 V(III), 4.5 V(IV), and discharged state

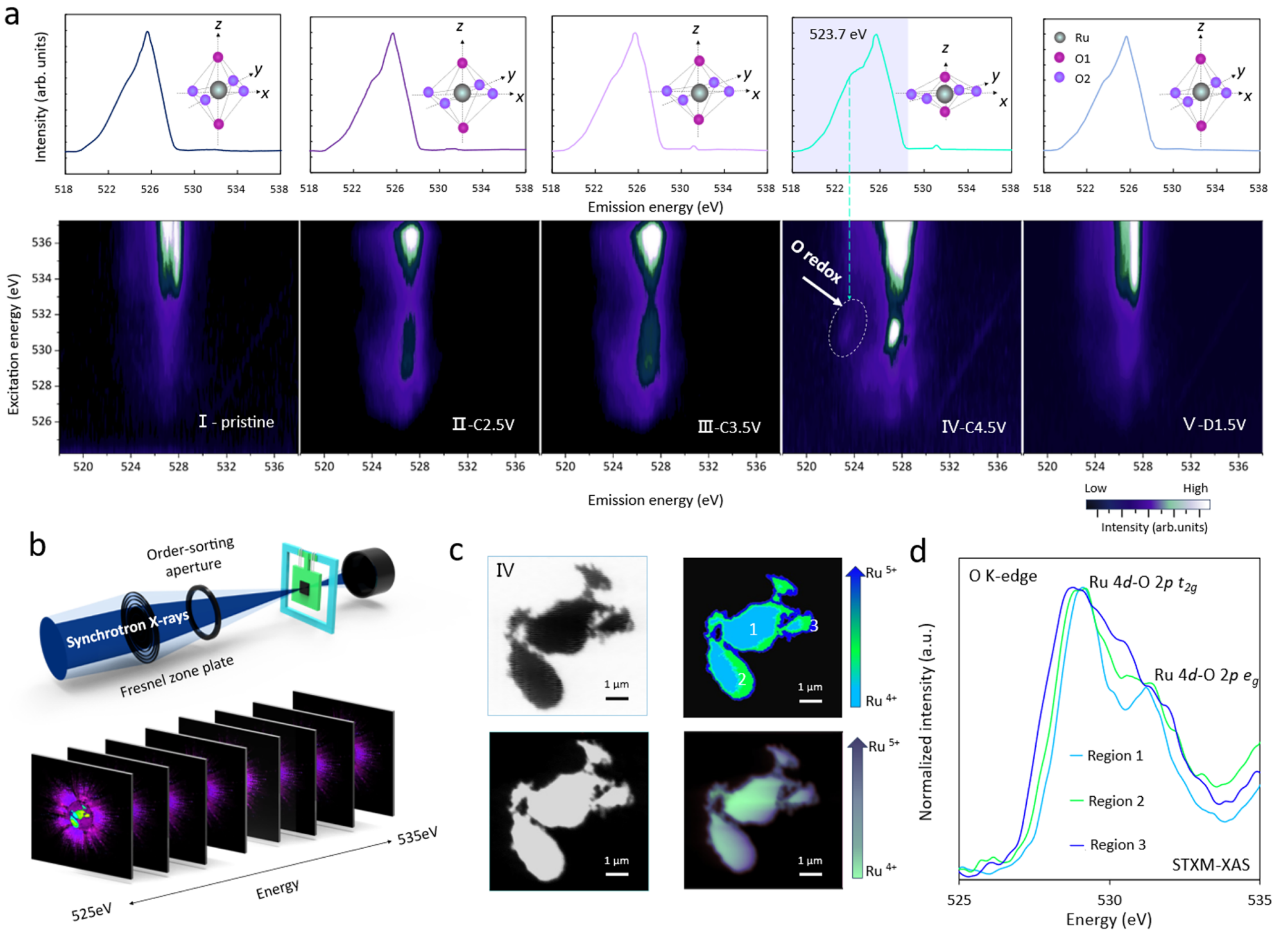

Fig. 5 | Switchable metal and oxygen redox centre in cascade catalysts. a O *K*-edge mRIXS results at various electrochemical states and homologous sPFY spectra integrated over the 523.7 eV emission-energy range. **b** Schematic representation of STXM-based soft X-ray Ptychography. **c** STXM morphology image of the charged $Na[Li_{1/3}Ru_{2/3}]O_2$ electrode, PCA appraisal (top), and RGB maps of oxygen (bottom). **d** STXM − XANES analysis of the O *K*-edge in different regions from (**c**).

1.5 V (V). It is challenging to detect the oxidation state of oxygen and distinguish it from the strong signals from Ru−O hybridization through traditional X-ray absorption spectrum. Thus, we studied the oxygen states before and after the charging via mapping of resonant inelastic X-ray scattering (mRIXS), a unique method for detecting oxygen oxidation to a non-divalent state. By measuring signals with emission energy near 523.7 eV and another excitation energy arround 531.0 eV (indicated by white arrows in Fig. 5a for the IV stage), we confirmed the oxidation of lattice O. The signal appeared at 3.5 V, intensified while charging to 4.5 V, and reversed upon discharging to 1.5 V (Fig. 5a). The evolution of the mRIXS characteristic on a catalytic cycle offers conclusive experimental certification for an invertible oxygen-redox reaction[53]. The oxygen oxidation signal reveals the lattice oxygen reactivity of catalysts, where $(O_2)^{n-}$ species are identified under a high voltage as marked in the white dashed circle. In the charged state, the signal of $(O_2)^{n-}$ species completely vanishes, which serves as the infrastructure for reversible electrocatalysis.

The spatial and chemical element distributions and nanoscale morphological information provide crucial insights into the dynamic catalytic mechanism. Scanning transmission X-ray microscopy (STXM) delivers significant evidence regarding the local bonding environment of components from the surface to the core within the charged electrode[54], as shown in Fig. 5b. The O *K*-edge STXM of charged $Na[Li_{1/3}Ru_{2/3}]O_2$ verifies the existence of oxygen-containing species. Principal Component Analysis (PCA) and RGB mapping of the absorption image stack from STXM further visualized the differences in the chemical distribution of oxygen between the above-mentioned electrode surface and bulk (Fig. 5c). The comparison of O *K*-edge STXM XAS at the different areas of the charged electrodes $Na[Li_{1/3}Ru_{2/3}]O_2$ is shown in Fig. 5d. The peaks observed around 529 eV and 532 eV are attributed to the t_{2g} and e_g unoccupied orbitals of hybridized O *2p*–Ru, respectively[55]. The e_g/t_{2g} ratio in the surface region (region 1) was lower than in the bulk (region 3), indicating fewer unoccupied orbitals. The gradual increase in O *K*-edge intensity from the surface to the bulk can be linked to the anionic redox, which differentiates it from RuO_2 (Supplementary Fig. 29). Partially occupied orbitals are crucial for improving electrocatalyst activity by promoting receiving and offering of electron, hence allowing the stimulation of molecular bonds for reaction intermediate.

The emergence of O-redox during electrochemical cycling could influence the cationic redox reactions. The alterations in the Ru valence state of $Na[Li_{1/3}Ru_{2/3}]O_2$ were assessed by analyzing the ex-situ X-ray absorption near edge structure XANES spectra (Supplementary Fig. 30). Based on the white-line energy of the standard reference samples (Supplementary Fig. 31), we found that Ru in $Na[Li_{1/3}Ru_{2/3}]O_2$ progressively oxidized from its initial 4+ state to 4.45+ at 3.5 V[56]. However, a shift of the absorption edge back to lower energy after charging to 4.5 V is attributed to the reductive coupling mechanism (RCM) of oxygen redox (Supplementary Fig. 32). Following discharging to 1.5 V, the edge returned to its original position, indicating that Ru was reduced to its initial valence state. With potential variations, when the metal d band intersects the oxygen p band at a higher potential, the redox center of the catalyst is no longer solely defined by the metal. Consequently, the catalytic activity could be continually enhanced by transitioning the active center of catalysts from primarily cationic to anionic redox activation.

Extended X-ray absorption fine structure (EXAFS) further indicates that Ru–O interatomic distances decreased. In contrast, Ru-Ru distances remained nearly constant when $Na[Li_{1/3}Ru_{2/3}]O_2$ was charged to high voltages (Supplementary Figs. 33 and 34). The EXAFS fitting results revealed a reduction in the Ru-O coordination number from 6 to 5 (Supplementary Fig. 35 and Table S6). The overall coordination number of the first Ru–O shell was restored during cycling, suggesting that the stretching vibration O–Ru–O arrangement is reversible[57]. This is consistent with the XPS analysis (Supplementary Fig. 36). With changes in potential, the oriented orbitals hybridize in two axes between the transition metal (TM) and oxygen (Supplementary Table S6). The unit cell in the coupled integrated catalysis undergoes reversible geometric transformation between octahedral and tetragonal forms of RuO_6, with Li^+ providing spatial localization (Fig. 5a, inset). Ru acts as a positive center throughout the cycles, forming a strong bond with the oxygen framework, which helps prevent oxygen loss at high cutoff voltages and maintains structural integrity during long-term cycling (Supplementary Table S7). The active metal sites in the cascade catalysts would experience a redox shift in their chemical states in response to reversing current during the charge and discharge processes.

The mechanism and reversibility of RuO_2 in sodium-air batteries using commercial RuO_2 as the electrode were investigated by ex-situ XRD, TEM, and XAS analyses, which revealed that crystalline RuO_2 transforms into an amorphous Ru/Na_2O mixture during discharge, and recharges back to amorphous RuO_2, highlighting its straightforward conversion behavior. This observation highlights the conversion-type behavior of RuO_2. It is important to note that the reversibility of this material is inferior to that of intercalated materials $Na[Li_{1/3}Ru_{2/3}]O_2$ (Supplementary Figs. 37–39).

Mechanism analysis

The experimental results unambiguously verify that the unusual reactivity is ascribed to the switchable active center for the redox of cations ($M^{n+} \rightleftarrows M^{(n+1)+}$) and anions ($2O^{2-} \rightleftarrows (O_2)^{n-}$) in $Na[Li_{1/3}Ru_{2/3}]O_2$. However, the relationship between its catalytic performance and the unique crystal/electronic structure remains unraveled. Transforming the M–O covalency by an in situ electrochemistry process can help adjust the d-band center (ε_d) energy level, a classical indicator for binding strength[58]. We thus established a correlation between overpotential and adsorption energy to act as a descriptor of the catalytic performance of the $Na[Li_{1/3}Ru_{2/3}]O_2$ catalysts. Density functional theory (DFT) calculations were implemented to evaluate the origin of the activity and scrutinize the adsorption energies between $Na[Li_{1/3}Ru_{2/3}]O_2$ and various products. The integrated-crystal orbital Hamilton population (ICOHP) represents the strength of chemical bonds[59]. The value of Ru-O adsorbed in Na_2CO_3 is −2.15 eV for C-4.5 V (Fig. 6a), which obvious is less than that of Ru-O in underpotential C-3.5 V with Na_2O_2 (−1.87) and C-2.5 V with NaO_2 (−1.55), indicating that Na_2CO_3 forms more stable and strong chemical bonds when adsorbed on the $Na[Li_{1/3}Ru_{2/3}]O_2$ surface at the charge 4.5 V.

The decomposition of adsorbed Na_2CO_3 can be understood as breaking the Na-O bond, resulting in the formation of individual Na atoms and $NaCO_3$ clusters. In this context, the COHP profiles have proved that the interaction between oxygen atoms in Na_2CO_3 and Ru atoms in $Na[Li_{1/3}Ru_{2/3}]O_2$ is quite strong. This strong interaction will stretch the Na-O bond in Na_2CO_3 and make it easier to be broken (Supplementary Fig. 40 and Table S8). Additional calculations were conducted on the density of states (DOS) of adsorbed several products and the 4*d* orbital and d band center for the Ru atom[60]. The *d*-band center of $Na[Li_{1/3}Ru_{2/3}]O_2$-4.5 V adsorbing Na_2CO_3 is at −1.60 eV, which is nearer to the Fermi energy in comparison to that of $Na[Li_{1/3}Ru_{2/3}]O_2$-3.5 V adsorbing Na_2O_2 (−1.73 eV) and $Na[Li_{1/3}Ru_{2/3}]O_2$-2.5 V adsorbing NaO_2 (−1.97 eV). In brief, the upwards shift of the Ru *d*-band center of $Na[Li_{1/3}Ru_{2/3}]O_2$ can reduce the electronic orbital occupation of anti-bonding states, resulting in a gradually increased adsorption energy for NaO_2, Na_2O_2, and Na_2CO_3 (Fig. 6b). The catalytic performance of RuO_2 through DFT calculations was also investigated. The *d*-band centers of RuO_2 at various charging states: −1.57 eV (C-2.5 V), −1.55 eV (C-3.5 V), and −1.51 eV (C-4.5 V). This stability suggests that the electronic properties of Ru remain consistent, limiting the formation of dynamic active centers. Density of states analysis indicates that the covalency of Ru-O bonds is also stable across charging states, with ICOHP values of −1.54, −1.68, and −1.71, confirming similar Ru-O interactions(Supplementary Fig. 41).

As adsorbent containing oxygen generally interacts with the *d* band of Ru atoms, the binding energies of NaO_2 and Na_2CO_3 depend proportionally on the *d*-band centers of catalyst active sites (Fig. 6c). The elevated position of $d_z{}^2$ electrons is ascribed to e_g orbitals, which orient vertically toward the O ligands of the adsorbate, promoting a significant spatial overlap between the O 2*p* orbital and the partially filled $d_z{}^2$ occupation orbital[61] (Supplementary Figs. 42 and 43). Hence, the $d_z{}^2$ electrons of the octahedral active site are crucial for the catalytic activity of SSNAB. Fig. 6d illustrates each reaction step's free energy competition for electron involvement (Supplementary Data 1 and 2). For the cascade catalyst, two catalytic models were designed to match the stepwise decomposition of Na_2O_2 and Na_2CO_3. Throughout the charging process, $Na[Li_{1/3}Ru_{2/3}]O_2$ exhibits a lower overpotential (0.207 V) compared to RuO_2 (-0.855 V), indicating that the dynamic variation of the d-band center in the cascade catalyst active sites can facilitate the decomposition of complex products[62]. Furthermore, charge density difference implying that the reaction occurs on the $Na[Li_{1/3}Ru_{2/3}]O_2$ sites with an abundance of electron transfers compared with the RuO_2 surface (Supplementary Figs. 44 and 45), which is coincident with dissociation energy of different adsorbent on $Na[Li_{1/3}Ru_{2/3}]O_2$ and RuO_2 (Supplementary Fig. 46). Moreover, a similar cascade catalytic reaction mechanism may also be achieved in other sodium-containing layered oxides (such as NLMO), confirming the universality of the Na-O-Li structural configuration of the electrode in realizing this mechanism in sodium-air batteries (Supplementary Figs. 47 and 48).

The investigation of redox switchable catalysis enables the formation of O-O bonds and provides ligand vacancies that extend beyond conventional metal sites, which is anticipated to enhance the catalytic efficiency for the complex products of SSNAB. Specifically, the high-spin active center, characterized by weak adsorption strength on NaO_2, facilitates subsequent desorption transformations. A moderately positioned *d*-band center with appropriate adsorption strength for Na_2O_2 helps to maintain a balance between absorption and desorption. In contrast, the low-spin state active center can stabilize the hard-to-decompose Na_2CO_3 through strong covalent interactions, allowing continuous transformation[63] (Fig. 6e). This approach introduces a versatile strategy for optimizing geometrical configurations to lower each oxygen redox step's energy barrier.

Discussion

In conclusion, our study has illustrated the merits of $Na[Li_{1/3}Ru_{2/3}]O_2$ as an efficient cascade catalyst for SSNAB. The noteworthy enhanced reactivity and reversibility observed in this system are achieved through modulation of Ru–O covalent interactions. Introducing Li dopants has proven effective in fine-tuning the RuO_6 distortion, forming varied degrees of e_g^* band broadening through controlled Na^+ occupation. The dynamic active sites could align their potential to the redox process during cycling, leading to the favourable catalytic reactivity for all the products. Within the potential region, the e_g^* band broadening could facilitate the affinity for NaO_2 desorption, thereby bolstering adsorption-desorption efficiency. Meanwhile, at elevated potentials where the rate-determining step involves Na_2O_2/

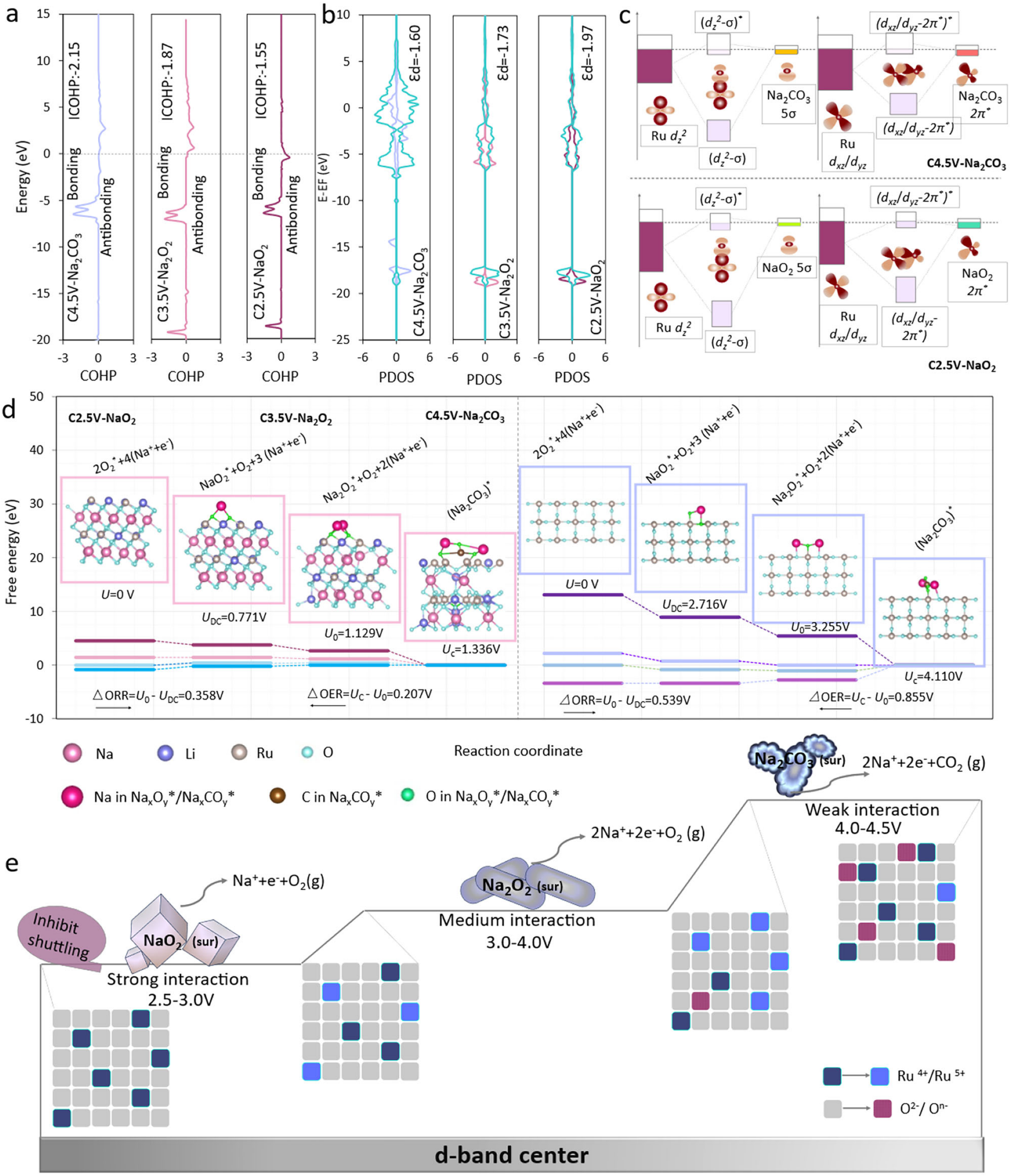

Fig. 6 | Schematic of the reaction Mechanism of cascade catalysis. **a** COHP of active Ru atom and coordination atom of different adsorbed species for C-2.5 V, C-3.5 V, and C-4.5 V of Na[Li$_{1/3}$Ru$_{2/3}$]O$_2$ electrodes. **b** The PDOS of adsorbed NaO$_2$, Na$_2$O$_2$, Na$_2$CO$_3$, and the 4*d* orbital of the Ru atom that is directly engaged in charging for C-2.5 V, C-3.5 V, and C-4.5 V, with corresponding Ru 4*d*-band center denoted by dashed lines. **c** Schematic representation of orbital interactions between NaO$_2$/ Na$_2$CO$_3$ and 4*d* orbital for C-2.5 V and C-4.5 V of Na[Li$_{1/3}$Ru$_{2/3}$]O$_2$ catalysts, respectively. **d** Gibbs free energy and activation energy analysis of varying electrochemical states Na[Li$_{1/3}$Ru$_{2/3}$]O$_2$ (left) and RuO$_2$ (right) electrodes. The insets are the optimized molecular structures at various steps, see Supplementary Data 1 and 2. **e** Schematic of a gradient catalytic system for regulating integrated SSNAB batteries. The divided squares in the schematic indicate the dynamic evolution process of different atomic valences.

Na_2CO_3 decomposition, the high-spin Ru^{4+} state transitions to a low-spin Ru^{5+} state in the e_g orbitals due to the loss of one electron. This transition enhances the adsorption capacity for oxygen-containing intermediates, reducing the thermodynamic barrier for the oxygen evolution reaction while improving the kinetic properties. Cascade catalysts have the potential to position different functionalities, which may help in controlling reaction intermediates. This could lead to unique characteristics in the catalysis process in SSNAB and may also open up opportunities for improvements in other energy storage areas.

Methods

Material synthesis

The layered $Na[Li_{1/3}Ru_{2/3}]O_2$ was prepared using conventional solid-state techniques[19]. Stoichiometric quantities of Na_2CO_3(Aladdin, 99%), Li_2CO_3 (Aladdin, 99%), and RuO_2 (Aladdin, 99.9%) were thoroughly blended and ground for thirty minutes using a mortar and pestle. The resultant powder was then shaped into pellets and calcined at 750 °C for 10 h in air, whereafter a second calcination at 900 °C in air for another 10 h, after which it was allowed to cool to room temperature naturally before being transferred into the glove box for further electrode preparation. $Na[Li_{1/3}Mn_{2/3}]O_2$ material was prepared from Na_2CO_3(Aladdin, 99%), Li_2CO_3 (Aladdin, 99%), and MnO_2 (Aladdin, 99.9%) precursor; the specific operation steps can be referred to in the above process.

$Na[Na_{1/3}Ru_{2/3}]O_2$ was synthesized through solid-state reactions using stoichiometric amounts of Na_2CO_3 (Aladdin, 99%) and RuO_2 (Aladdin, 99.9%), with an additional 5 mol% Na_2CO_3. These components were thoroughly combined and ground. The resulting powder was pelletized and calcined at 900 °C for 10 h under an argon atmosphere[51].

Electrolyte preparation

Poly(vinylidene fluoride-co-hexafluoropropylene)(PVDF-HFP) powders and sodium salts were dried at 100 °C for 12 h before use to remove trapped water. PVDF-HFPpolymer (1.5 g; Sigma-Aldrich) was mixed in 15 mL of acetone(Aladdin, ≥98%) containing 10 wt% fumed silica and heated at 50 °C for 2 h with stirring, then rested for 1 h to remove bubbles. The mixture solution was distributed as a film on a watch glass and dried at 60 °C overnight using a vacuum chamber. In another beaker, liquid electrolytes were prepared by dissolving $NaClO_4$ salts (Aladdin, ≥99.99%) in tetraethylene glycol dimethyl ether (TEGDME, ≥99.5%) by magnetic stirring at 700 rpm for 12 h in a glovebox under argon atmosphere. Molarities were adjusted to 1 M electrolyte. Subsequently, TEGDME with dissolved sodium salts and PVDF-HFP solution was mixed, where the mass ratio of PVDF-HFP solution to liquid electrolyte was adjusted as 7:2, and a quasi-solid electrolyte (QPE) membrane was obtained.

Electrochemical measurements

Nickel foam was punched into circular electrode sheets with a diameter of 12 mm, cleaned in 1 M HCl solution for 30 min, and then thoroughly washed with deionized water/ethanol successively to remove the residual chloride ions. A pristine electrode was produced by coating nickel foam with a uniform ink containing 90 wt% $Na[Li_{1/3}Ru_{2/3}]O_2$ powder and 10 wt% PVDF-HFP binder mixture in 5 ml N-Methyl pyrrolidone (Aladdin, 98%) to ensure uniform dispersion, enhancing battery performance. This solution was dispersed evenly with a nickel foam collector (Youveim, purity:>99.9%, thickness mm, porosity:98%, areal density: 280 gm^{-2}) by ultrasonic instrument (KQ-400KDE), dried under vacuum for 12 h, achieving a mass loading of approximately 0.5 mg cm^{-2}. Post-casting, the electrodes were dried at 80 °C overnight inside a vacuum environment. One side of the air electrode was in contact with the electrolyte, and the other was exposed to ambient air as an oxygen source. Batteries were assembled in an argon-filled glovebox (O_2 and H_2O contents <0.1 ppm) using 2032-type coin cells, layering the Na metal sheet (China Energy Lithium Co., Ltd, diameter:14 mm, thickness: 0.45 mm), a 16 mm composite electrolyte film containing $NaClO_4$/TEGDME, and the electrode sequentially. The electrochemical tests were conducted using a NEWARE Battery Test System (CT-4008T-5V50mA-164, Shenzhen, China) under various parameters in ambient air (25 °C, relative humidity:20%)[64]. The CV tests were conducted over a potential scan range of 1.5 to 4.5 V (vs. Na^+/Na) at a scan rate of 0.1 mVs^{-1}, with a sodium foil serving as the counter electrode and reference electrode. Electrochemical impedance spectroscopy (EIS) was carried out with an impedance analyser at open circuit voltage with an AC oscillation of 0.01 V amplitude over frequencies from 850 kHz to 0.1 Hz.

Assembly of solid-state pouch batterie

The solid-state soft pack battery assembled in this study is pouch-type. Foam nickel coated (8 × 8 cm^2) with a catalyst serves as the air electrode (mass loading: 10 mg cm^{-2}), while sodium strips (8 × 8 cm^2) are used as the anode. Aluminum tabs are used for the positive electrode, and nickel tabs for the negative electrode. Quasi-solid polymer electrolyte acts as the solid electrolyte (10 × 10 cm^2). The entire battery assembly process is conducted in an argon-filled glove box, where the electrode sheet, solid electrolyte, and anode sheet are stacked in order and vacuum sealed with a perforated aluminum-plastic film. The performance testing of the completed solid-state soft pack battery is carried out under ambient air conditions.

Material characterization

The substance's composition was analyzed using a range of characterization techniques, including XRD (PANalytical Empyrean), XPS (KRATOS AXIS Ultra DLD), Raman (inVia-Reflex), SEM (ZEISS Merlin Compact; Phenom Pro), in situ differential electrochemical mass spectrometry (DEMS, Hiden Analytical), and ICP-MS (PerkinElmer, Optima 5300DV).

O K-edge resonant inelastic X-ray scattering (RIXS)

mRIXS was performed at Beamline BL20U1 and BL20U2 of the Shanghai Synchrotron Radiation Facility (SSRF). The mapping data were obtained using a highly efficient modular spectrometer with an excitation energy increment of 0.2 eV. The final two-dimensional maps were generated through a multistep data processing approach, as detailed in a prior study[65].

Scanning transmission X-ray microscopy (STXM)

The STXM measurements were conducted at the beamline. BL08U1A of SSRF. The grids were placed in a sample holder, sealed in an aluminum pouch, and transported to the beamline. STXM images were obtained with an 8 × 8 μm^2 scanned (200 × 200 points) image size with a step size of 0.04 µm, and setting a dwell time of 1 ms per pixel, followed by PCA-CA analysis to identify natural spectrum groups and calculate average spectra[66].

XAFS measurements

XAS spectra were recorded at beamline BL14W1 of SSRF for the Ru K-edge. Samples were prepared by cycling the electrode to the desired voltage and transporting them to the beamline in an argon-filled bag to protect against moisture and oxygen. Data analysis was conducted with the Athena software, with EXAFS fittings done via the Artemis program[51].

HAADF-STEM and EELS

TEM, HR-TEM, atomic resolution-HAADF-STEM images, and EELS were obtained employing the aberration-corrected JEM-ARM200F(C)[67].

TOF-SIMS

The Time-of-Flight Secondary Ion Mass Spectrometry (TOF-SIMS) (IONTOF GmbH, Münster, Germany) was employed. The 3D data was obtained in an area of 15 × 15 µm. The measurements were conducted in negative modes[40].

SQUID magnetometry

Susceptibility experiments were implemented in zero-field cooling mode by a SQUID XL magnetometer with 1 T implemented fields from 0 to 200 K. Powder samples were sealed in vacuum quartz tubes with cotton to prevent movement. EPR spectra were recorded on a Bruker Elexsys E580 spectrometer (ω = 9.36 GHz)[48].

Solid-state ^{23}Na and ^{7}Li MAS NMR spectroscopy

Solid-state NMR experiments for ^{23}Na were conducted on a WB 14.1 T Bruker ADVANCE III spectrometer. Spectra were collected at spinning frequencies of 15 kHz using the Hahnecho pulse sequence. For ^{7}Li, measurements were conducted on a WB 11.75 T spectrometer with a Larmor frequency of 194.3 MHz[52].

Computational details

DFT calculations were implemented employing the Vienna ab initio simulation package with the Perdew-Burke-Ernzerhof functional for exchange-correlation interactions. A plane-wave basis set featuring a kinetic energy cutoff of 400 eV, energy convergence criterion of 10^{-5} eV, force convergence criterion of 0.02 eV Å^{-1}, and (2 × 2 × 1) Monkhorst–Pack *k*-point sampling were adopting for structure relaxation. The $Na[Li_{1/3}Ru_{2/3}]O_2$ system was modeled by substituting Ru ions with Li ions in a cell containing 16 formula units[60].

Data availability

All data supporting this work are available in the article and its Supplementary Information or are available from the corresponding authors upon request. Source data are provided with this paper.

References

1. Bruce, P. G., Freunberger, S. A., Hardwick, L. J. & Tarascon, J.-M. Erratum: Li–O2 and Li–S batteries with high energy storage. *Nat. Mater.* **11**, 172–172 (2011).
2. Hartmann, P. et al. A rechargeable room-temperature sodium superoxide (NaO_2) battery. *Nat. Mater.* **12**, 228–232 (2012).
3. Xia, C., Black, R., Fernandes, R., Adams, B. & Nazar, L. F. The critical role of phase-transfer catalysis in aprotic sodium oxygen batteries. *Nat. Chem.* **7**, 496–501 (2015).
4. Ma, J. -l. et al. Prevention of dendrite growth and volume expansion to give high-performance aprotic bimetallic Li-Na alloy–O_2 batteries. *Nat. Chem.* **11**, 64–70 (2018).
5. Hu, Y. Y. et al. Origin of additional capacities in metal oxide lithium-ion battery electrodes. *Nat. Mater.* **12**, 1130–1136 (2013).
6. Qiao, Y., Jiang, K., Deng, H. & Zhou, H. A high-energy-density and long-life lithium-ion battery via reversible oxide–peroxide conversion. *Nat. Catal.* **2**, 1035–1044 (2019).
7. Wang, X. et al. Achieving a high-performance sodium-ion pouch cell by regulating intergrowth structures in a layered oxide electrode with anionic redox. *Nat. Energy.* **9**, 184–196 (2024).
8. Mortemard de Boisse, B. et al. Intermediate honeycomb ordering to trigger oxygen redox chemistry in layered battery electrode. *Nat. Commun.* **7**, 11397 (2016).
9. Huang, Z.-F. et al. Tuning of lattice oxygen reactivity and scaling relation to construct better oxygen evolution electrocatalyst. *Nat. Commun.* **12**, 3992 (2021).
10. Ye, L. et al. A rechargeable calcium–oxygen battery that operates at room temperature. *Nature* **626**, 313–318 (2024).
11. Ben Yahia, M., Vergnet, J., Saubanère, M. & Doublet, M.-L. Unified picture of anionic redox in Li/Na-ion batteries. *Nat. Mater.* **18**, 496–502 (2019).
12. Dong, T. et al. How do polymer binders assist transition metal oxide electrodes to address the challenge of high-voltage lithium battery applications?. *Electrochem. Energy Rev.* **4**, 545–565 (2021).
13. Wang, X.-X. et al. Metal–organic framework-based mixed conductors achieve highly stable photo-assisted solid-state lithium–oxygen batteries. *J. Am. Chem. Soc.* **145**, 5718–5729 (2023).
14. Hao, H. et al. Molybdenum carbide electrocatalyst in situ embedded in porous nitrogen-rich carbon nanotubes promotes rapid kinetics in sodium-metal–sulfur batteries. Adv. Mater. 34, e2106572 (2022).
15. Liu, S. et al. Atomically dispersed iron sites with a nitrogen–carbon coating as highly active and durable oxygen reduction catalysts for fuel cells. *Nat. Energy* **7**, 652–663 (2022).
16. Park, H. et al. Activating reversible carbonate reactions in Nasicon solid electrolyte-based Na-air battery via in-situ formed catholyte. *Nat. Commun.* **15**, 2952 (2024).
17. Xiong, Q., Huang, G. & Zhang, X. B. High-capacity and stable Li-O_2 batteries enabled by a trifunctional soluble redox mediator. *Angew. Chem. Int. Ed.* **59**, 19311–19319 (2020).
18. Xie, H. et al. Ta–TiO_x nanoparticles as radical scavengers to improve the durability of Fe–N–C oxygen reduction catalysts. *Nat. Energy* **7**, 281–289 (2022).
19. Wang, Q. et al. Unlocking anionic redox activity in O3-type sodium 3 d layered oxides via Li substitution. *Nat. Mater.* **20**, 353–361 (2021).
20. Wu, Z. et al. Realizing high capacity and zero strain in layered oxide electrodes via lithium dual-site substitution for sodium-ion batteries. *J. Am. Chem. Soc.* **145**, 9596–9606 (2023).
21. Zhao, S. et al. Bifunctional effects of cation additive on Na-O_2 batteries. *Angew. Chem. Int. Ed.* **60**, 3205–3211 (2020).
22. Liu, Y. et al. Metal–organic framework-derived hierarchical Co_3O_4@$MnCo_2O_{4.5}$ nanocubes with enhanced electrocatalytic activity for Na–O_2 batteries. *Nanoscale* **11**, 5285–5294 (2019).
23. Li, N. et al. Enabling pyrochlore-type oxides as highly efficient electrocatalysts for high-capacity and stable Na–O_2 batteries: the synergy of electronic structure and morphology. *ACS Catal.* **7**, 7688–7694 (2017).
24. Kwak, W.-J. et al. Nanoconfinement of low-conductivity products in rechargeable sodium–air batteries. *Nano Energy* **12**, 123–130 (2015).
25. Hu, Y. et al. Porous perovskite calcium–manganese oxide microspheres as an efficient catalyst for rechargeable sodium–oxygen batteries. *J. Mater. Chem. A* **3**, 3320–3324 (2015).
26. Yin, W.-W. et al. A long-life Na–air battery based on a soluble NaI catalyst. *Chem. Commun.* **51**, 2324–2327 (2015).
27. Chang, S. et al. High-performance quasi-solid-state Na-air battery via gel electrode by confining moisture. Adv. Funct. Mater. 31, 2011151 (2021).
28. Zhang, S. et al. Graphene nanosheets loaded with Pt nanoparticles with enhanced electrochemical performance for sodium–oxygen batteries. *J. Mater. Chem. A* **3**, 2568–2571 (2015).
29. Ma, J. -l. et al. Synthesis of porous and metallic CoB nanosheets towards a highly efficient electrocatalyst for rechargeable Na–O_2 batteries. *Energy Environ. Sci.* **11**, 2833–2838 (2018).
30. Khan, Z. et al. Three-dimensional SnS_2 nanopetals for hybrid sodium-air batteries. Electrochim Acta. **257**, 328–334 (2017)
31. Kim, M., Ju, H. & Kim, J. Single crystalline $Bi_2Ru_2O_7$ pyrochlore oxide nanoparticles as efficient bifunctional oxygen electrocatalyst for hybrid Na-air batteries. *Chem. Eng. J.* **358**, 11–19 (2019).
32. Kang, Y. et al. Novel high-energy-density rechargeable hybrid sodium–air cell with acidic electrolyte. *ACS Appl. Mater. Interfaces* **10**, 23748–23756 (2018).
33. Lin, X. et al. Reviving anode protection layer in Na-O_2 batteries: failure mechanism and resolving strategy. *Adv. Energy Mater.* **11**, 2003789–2003797 (2021).

34. Sun, B. et al. Hierarchical porous carbon spheres for high-performance Na–O_2 batteries. *Adv. Mater.* **29**,1606816–1606823 (2017).
35. Liu, X., Lei, X., Wang, Y.-G. & Ding, Y. Prevention of Na corrosion and dendrite growth for long-life flexible Na–air batteries. *ACS Cent. Sci.* **7**, 335–344 (2021).
36. Yin, W.-W. & Fu, Z.-W. A highly efficient bifunctional heterogeneous catalyst for morphological control of discharged products in Na–air batteries. *Chem. Commun.* **53**, 1522–1525 (2017).
37. Liu, Y. et al. Uncovering the geometry activity of spinel oxides in Li-CO_2 battery reactions. *ACS Energy Lett.* **9**, 2173–2181 (2024).
38. Su, Z. et al. X-ray nanocomputed tomography in Zernike phase contrast for studying 3D morphology of Li-O_2 battery electrode. *Acs Appl. Energy Mater.* **3**, 4093–4102 (2020).
39. Pang, Y., Pan, J., Yang, J., Zheng, S. & Wang, C. Electrolyte/electrode interfaces in all-solid-state lithium batteries: a review. *Electrochem. Energy Rev.* **4**, 169–193 (2021).
40. Yu, W. et al. A volatile redox mediator boosts the long-cycle performance of lithium-oxygen batteries. *Energy Storage Mater.* **38**, 571–580 (2021).
41. Bi, X., Wang, R., Amine, K. & Lu, J. A critical review on superoxide-based sodium–oxygen batteries. *Small Methods.* **3**, 1800247–1800254 (2018).
42. Dubouis, N. et al. Extending insertion electrochemistry to soluble layered halides with superconcentrated electrolytes. *Nat. Mater.* **20**, 1545–1550 (2021).
43. Ning, F. et al. Inhibition of oxygen dimerization by local symmetry tuning in Li-rich layered oxides for improved stability. *Nat. Commun.* **11**, 4973–4984 (2020).
44. Yadegari, H. et al. On rechargeability and reaction kinetics of sodium–air batteries. *Energy Environ. Sci.* **7**, 3747–3757 (2014).
45. Gao, R. et al. Probing the self-boosting catalysis of $LiCoO_2$ in Li–O_2 battery with multiple in situ/operando techniques. *Adv. Funct. Mater.* **30**, 2002223–2002232 (2020).
46. Wang, C. et al. Resolving complex intralayer transition motifs in high-Ni-content layered electrode materials for lithium-ion batteries. *Nat. Mater.* **22**, 235–241 (2023).
47. Li, L. et al. Fluorination-enhanced surface stability of disordered rocksalt electrodes. Adv. Mater. 34, e2106256 (2022).
48. Zuo, Y. et al. Regulating the potential of anion redox to reduce the voltage hysteresis of Li-rich electrode materials. *J. Am. Chem. Soc.* **145**, 5174–5182 (2023).
49. Zhong, H. et al. Key role of eg* band broadening in nickel-based oxyhydroxides on coupled oxygen evolution mechanism. *Nat. Commun.* **14**, 7488 (2023).
50. Yao, Y. et al. The effect of electrochemically inactive Ti substituted for Ru in Li_2RuTiO_3 on structure and electrochemical performance. *J. Energy Chem.* **60**, 222–228 (2021).
51. Cao, X. et al. Triggering and stabilizing oxygen redox chemistry in layered $Li[Na_{1/3}Ru_{2/3}]O_2$ enabled by stable Li–O–Na configuration. *ACS Energy Lett.* **7**, 2349–2356 (2022).
52. Carlier, D., Ménétrier, M., Grey, C. P., Delmas, C. & Ceder, G. Understanding the NMR shifts in paramagnetic transition metal oxides using density functional theory calculations. Phys. Rev. B **67**, 174103 (2003).
53. Zhuo, Z. et al. Cycling mechanism of Li_2MnO_3: Li–CO_2 batteries and commonality on oxygen redox in electrode materials. *Joule* **5**, 975–997 (2021).
54. Mefford, J. T. et al. Correlative operando microscopy of oxygen evolution electrocatalysts. *Nature* **593**, 67–73 (2021).
55. Eum, D. et al. Coupling structural evolution and oxygen-redox electrochemistry in layered transition metal oxides. *Nat. Mater.* **21**, 664–672 (2022).
56. Wang, H., An, H. W., Shan, H. M., Zhao, L. & Wang, J. J. Research progress on interfaces of all-solid-state batteries. Acta Phys.-Chim. Sin. 37, 2007070 (2021).
57. Sun, X. et al. Tailoring electronic-ionic local environment for solid-state Li-O_2 battery by engineering crystal structure. *Sci. Adv.* **8**, eabq6261 (2022).
58. Hwang, J. et al. Perovskites in catalysis and electrocatalysis. *Science* **358**, 751–756 (2017).
59. Zhu, Y. et al. Lattice engineering on Li2CO3-based sacrificial electrode prelithiation agent for improving the energy density of Li-ion battery full-cell. Adv. Mater. **36**, e2312159 (2023).
60. Tian, J. et al. Sabatier relations in electrocatalysts based on high-entropy alloys with wide-distributed d-band centers for Li-O_2 batteries. *Angew. Chem. Int. Ed.* **62**, e202310894 (2023).
61. Wang, X. et al. Pivotal role of reversible NiO_6 geometric conversion in oxygen evolution. *Nature* **611**, 702–708 (2022).
62. Benti, N. E. et al. The effect of CO_2 contamination in rechargeable non-aqueous sodium–air batteries. *J. Chem. Phys.* **152**, 074711 (2020).
63. Fu, Y. et al. dz^2 band links frontier orbitals and charge carrier dynamics of single-atom cocatalyst-aided photocatalytic H_2 production. *J. Am. Chem. Soc.* **145**, 28166–28175 (2023).
64. Zhu, Y., Yang, F., Guo, M., Chen, L. & Gu, M. Real-time imaging of the electrochemical process in Na–O2 nanobatteries using Pt@CNT and Pt0.8Ir0.2@CNT air electrodes. *ACS Nano* **13**, 14399–14407 (2019).
65. Ji, H. et al. Ultrahigh power and energy density in partially ordered lithium-ion electrode materials. *Nat. Energy* **5**, 213–221 (2020).
66. Li, M. et al. Ion–dipole-interaction-induced encapsulation of free residual solvent for long-cycle solid-state lithium metal batteries. *J. Am. Chem. Soc.* **145**, 25632–25642 (2023).
67. Zhang, F. et al. Surface regulation enables high stability of single-crystal lithium-ion electrodes at high voltage. *Nat. Commun.* **11**, 3050 (2020).

Acknowledgements

This work was supported by the National Natural Science Foundation of China (No. 92372110 and No. 22075063), the Chinesisch-Deutsches Mobilitätspropgamm (M-0281), the Fundamental Research Funds for the Central (Grant No. HIT.OCEF.2023039), the Heilongjiang Touyan Team (HITTY-20190033), the 'Young Scientist Studio' of Harbin Institute of Technology (HIT), the funds from Chongqing Research Institute of HIT, and funds from Suzhou Research Institute of HIT. We thank the National Key Research and Development Program of China(2022YFE0138900), the Natural Science Fund for Distinguished Young Scholars of Chongqing (cstc2021jcyj-jqX0003), "Young Scientist Studio" of Harbin Institute of Technology (HIT), and funds from Chongqing Research Institute of HIT. We thank the beamline BL13W1 at SSRF for micro-CT measurements, beamline BL20U1 and BL20U2 at SSRF for RIXS measurements, beamline BL08U1A at SSRF for STXM, and 4W1A beamline of Beijing Synchrotron Radiation Facility.

Author contributions

J.W. conceived and designed the experiments. X.S. undertook the materials synthesis, characterization, and performance testing. X.L. and P.J. performed the HAADF-STEM. Y.S. contributed to the DFT calculations. J.L. and H.L. assisted with the RIXS and STXM. B.D. and Q.L. assisted with the micro-CT test. M.L. assisted with the NMR. X.Z. assisted with the XAFS analysis. J.W. and D.S. assisted with data analysis and paper revision. All the authors discussed and revised the paper.

Competing interests

The authors declare no competing interests.

Additional information

Supplementary information The online version contains supplementary material available at https://doi.org/10.1038/s41467-025-60840-z.

Correspondence and requests for materials should be addressed to Dong Su or Jiajun Wang.

Peer review information *Nature Communications* thanks Feng Liang and the other, anonymous, reviewer(s) for their contribution to the peer review of this work. [A peer review file is available].

Reprints and permissions information is available at http://www.nature.com/reprints

Publisher's note Springer Nature remains neutral with regard to jurisdictional claims in published maps and institutional affiliations.

Open Access This article is licensed under a Creative Commons Attribution-NonCommercial-NoDerivatives 4.0 International License, which permits any non-commercial use, sharing, distribution and reproduction in any medium or format, as long as you give appropriate credit to the original author(s) and the source, provide a link to the Creative Commons licence, and indicate if you modified the licensed material. You do not have permission under this licence to share adapted material derived from this article or parts of it. The images or other third party material in this article are included in the article's Creative Commons licence, unless indicated otherwise in a credit line to the material. If material is not included in the article's Creative Commons licence and your intended use is not permitted by statutory regulation or exceeds the permitted use, you will need to obtain permission directly from the copyright holder. To view a copy of this licence, visit http://creativecommons.org/licenses/by-nc-nd/4.0/.

© The Author(s) 2025